



# Six-beam homodyne laser Doppler vibrometry based on silicon photonics technology

YANLU LI,<sup>1,2,\*</sup> JINGHAO ZHU,<sup>1,2</sup> MATTHIEU DUPERRON,<sup>3</sup> PETER O'BRIEN,<sup>3</sup>  
RALF SCHÜLER,<sup>4</sup> SOREN AASMUL,<sup>5</sup> MIRKO DE MELIS,<sup>5</sup> MATHIAS  
KERSEMANS,<sup>6</sup> AND ROEL BAETS<sup>1,2</sup>

<sup>1</sup>Photonics Research Group, Ghent University-imec, Technologiepark-Zwijnaarde 15, 9052, Ghent, Belgium

<sup>2</sup>Center for Nano- and Biophotonics, Ghent University, Technologiepark-Zwijnaarde 15, 9052, Ghent, Belgium

<sup>3</sup>Photonic Packaging Group, Tyndall National Institute, Lee Maltings Complex Dyke Parade, T12R5CP, Cork, Ireland

<sup>4</sup>SIOS Messtechnik GmbH, Am Vogelherd 46, 98693, Ilmenau, Germany

<sup>5</sup>Medtronic Bakken Research Center, Endepolsdomein 5, 6229 GW, Maastricht, The Netherlands

<sup>6</sup>Department of Materials, Textiles and Chemical Engineering, Ghent University, Technologiepark-Zwijnaarde 903, 9052, Ghent, Belgium

\*Yanlu.Li@UGent.be

**Abstract:** This paper describes an integrated six-beam homodyne laser Doppler vibrometry (LDV) system based on a silicon-on-insulator (SOI) full platform technology, with on-chip photo-diodes and phase modulators. Electronics and optics are also implemented around the integrated photonic circuit (PIC) to enable a simultaneous six-beam measurement. Measurement of a propagating guided elastic wave in an aluminum plate (speed  $\approx 909$  m/s @ 61.5 kHz) is demonstrated.

© 2018 Optical Society of America under the terms of the [OSA Open Access Publishing Agreement](#)

**OCIS codes:** (280.0280) Remote sensing and sensors; (120.7280) Vibration analysis.

## References and links

1. A. Campo, G. Dudzik, J. Apostolakis, A. Waz, P. Nauleau, K. Abramski, J. Dirckx, and E. Konofagou, "Comparison between multi-channel LDV and PWI for measurement of pulse wave velocity in distensible tubes: Towards a new diagnostic technique for detection of arteriosclerosis," *Opt. Lasers Eng.* **97**, 41–51 (2017).
2. P. Chiariotti, M. Martarelli, and P. Castellini, "Exploiting Continuous Scanning Laser Doppler Vibrometry in timing belt dynamic characterization," *Mechanical Systems and Signal Processing*, Volume 86, Part B **1**, 66–81 (2017).
3. E. Sirevaag, S. Casaccia, E. Richter, J. O'Sullivan, L. Scalise, and J. Rohrbaugh, "Cardiorespiratory interactions: Noncontact assessment using laser Doppler vibrometry," **53**, 847–867 (2016).
4. N. Roozen, L. Labelle, M. Rychtáriková, and C. Glorieux, "Determining radiated sound power of building structures by means of laser Doppler vibrometry," *J. Sound Vibrat.* **346**, 81–99 (2015).
5. J. Posada-Roman, D. Jackson, M. Cole, and J. Garcia-Souto, "Multichannel fiber laser Doppler vibrometer studies of low momentum and hypervelocity impacts," *Opt. Lasers Eng.* (article in press).
6. Y. Fu, M. Guo, and P. B. Phua, "Spatially encoded multibeam laser Doppler vibrometry using a single photodetector," *Opt. Lett.* **35**(9), 1356–1358 (2010).
7. Y. Li, P. Segers, J. Dirckx, and R. Baets, "On-chip laser Doppler vibrometer for arterial pulse wave velocity measurement," *Biomed. Opt. Express* **4**(7), 1229–1235 (2013).
8. Y. Li and R. Baets, "Homodyne laser Doppler vibrometer on silicon-on-insulator with integrated 90 degree optical hybrids," *Opt. Express* **21**(11), 13342–13350 (2013).
9. "Europractice IC Service/Silicon Photonics MPW," [http://europractice-ic.com/SiPhotonics\\_general.php](http://europractice-ic.com/SiPhotonics_general.php)
10. D. Thomson, A. Zikie, J. Bowers, T. Komljenovic, G. Reed, L. Vivien, D. Marris-Morini, E. Cassan, L. Virof, J. Fédéli, J. Hartmann, J. Schmid, D. Xu, F. Boeuf, P. O'Brien, G. Mashanovich, and M. Nedeljkovic, "Roadmap on silicon photonics," *J. Opt.* **18**(7), 073003 (2016).
11. Y. Li, S. Verstyuyft, G. Yurtsever, S. Keyvaninia, G. Roelkens, D. Van Thourhout, and R. Baets, "Heterodyne laser Doppler vibrometers integrated on silicon-on-insulator with thermo-optic based frequency shifters," *Appl. Opt.* **52**, 2145–2152 (2013).
12. A. Dräbenstedt, J. Sauer, and C. Rembe, "Remote-sensing vibrometry at 1550 nm wavelength," *AIP Conf. Proc.* **1457**, 113–121 (2012).

13. Y. Li, L. Li, B. Tian, G. Roelkens, and R. Baets, "Reflectionless tilted grating couplers with improved coupling efficiency based on a silicon overlay," IEEE Photonics Technol. Lett. **25**(13), 1195–1198 (2013).
14. V. Giurgiutiu, "Tuned lamb wave excitation and detection with piezoelectric wafer active sensors for structural health monitoring," J. Intell. Mater. Syst. Struct. **16**(4), 291–305 (2005).
15. J. Rose, *Ultrasonic Waves in Solid Media* (Cambridge University, 1999).

## 1. Introduction

Based on coherent detection techniques, laser Doppler vibrometry (LDV) shows great vibration measurement accuracy with sub-nanometer resolution. The applications of LDV have been reported in various fields, e.g. in bio-medical engineering and mechanics [1–4]. The basic configuration of an LDV is an optical interferometer, which sends one laser beam (measurement signal) to the moving target and collects the corresponding reflection. Thanks to the Doppler effect, the relationship between the frequency shift of the reflected signal  $f_{Doppler}(t)$  and the out-of-plane velocity of the target  $v(t)$  is given by

$$f_{Doppler}(t) = 2v(t)/\lambda_0 \quad (1)$$

where  $\lambda_0$  is the light wavelength. To extract the Doppler shift, the reflected signal is coherently mixed with a reference signal before reaching a photo-diode (PD). The photocurrent of the mixture signal can be expressed as follows

$$\begin{aligned} sig(t) &= \kappa \left| a \cdot \exp[i \cdot (2\pi f_0 t + \varphi)] + b \cdot \exp \left[ i \cdot 2\pi \int_0^t f_{Doppler}(t) dt \right] \right|^2 \\ &= dc + r \cdot \cos \left[ 2\pi f_0 t - \theta_{Doppler}(t) + \varphi \right] \end{aligned} \quad (2)$$

where  $\kappa$  is a factor considering both the PD responsivity and optical losses,  $a$  and  $b$  are the amplitudes of the reference and measurement signals, respectively,  $f_0$  and  $\varphi$  are the constant frequency difference and phase difference between the reference and measurement signals, respectively,  $\theta_{Doppler}(t) = 2\pi \int_0^t f_{Doppler}(t) dt$  is the phase shift of the reflected signal caused by the Doppler effect,  $dc = \kappa (|a|^2 + |b|^2)$  is the dc part of the photocurrent, and  $r = 2\kappa ab$  is the amplitude of the ac part of the photocurrent. It can be derived that the instantaneous frequency of the ac part is  $f_0 - f_{Doppler}(t)$ . The system is usually called a homodyne vibrometry when  $f_0 = 0$ . Otherwise, it is called a heterodyne vibrometry. One important advantage of the heterodyne detection is that the electronic 1/f noise can be filtered out when the carrier frequency of useful measurement signals  $f_0$  is high enough (e.g. several MHz). Therefore, heterodyne vibrometry usually has a higher signal-to-noise ratio (SNR) than homodyne vibrometry. However, homodyne vibrometry still has a lot of applications thanks to its simpler configuration, since it doesn't generate two frequencies. Our demonstrated device is based on homodyne vibrometry.

In some cases [2], it is crucial to obtain the vibration information at multiple positions simultaneously, which is not easy for a commonly used single-point LDV system. To realize such measurements, two techniques are generally used: scanning LDV [2] and multi-beam LDV [1,5]. Scanning LDV systems are used more often thanks to their flexibility and simplicity compared to the multi-beam LDV systems. However, the performance of the scanning LDV is limited by its scanning frequency, which usually cannot reach the MHz range due to mechanics-based scanning devices. Therefore, common scanning LDV cannot detect a transient movement event, such as an impact. On the contrary, multi-beam LDV has no such limitations and it can measure transient and non-periodic events. Because multiple separate LDV devices are implemented in the same system, a multi-beam LDV system is usually more bulky and complex. But some solutions emerged recently. For example, Fu et al. demonstrated a spatially encoded multi-beam heterodyne LDV by simultaneously using the multiple diffraction beams from the acousto-optic modulator [6].

As we have proposed previously [7,8], silicon-on-insulator (SOI) photonic integration technology can be used to realize miniaturized and low-cost multi-beam LDVs. Current SOI-based silicon photonics platforms (e.g. europractice [9]) include many compact optical components (e.g. filters, couplers, modulators, and PDs) that can be used in various telecom and sensing applications [10]. Based on this technology, we have already demonstrated a heterodyne LDV PIC with a kHz-range frequency shifter based on a thermo-optic phase modulator [11], a homodyne LDV assisted with a 90-degree optical hybrid [8], and a two-beam homodyne LDV which enables the pulse-wave-velocity measurement of common carotid arteries [7]. In this paper, a six-beam LDV is demonstrated. With more than two beams, the LDV can realize a better analysis of the vibration modes of the targets. Unlike the previous demonstrations which used external PDs, the new six-beam LDV takes advantage of the integrated germanium PDs realized on the SOI platform. The integrated PDs help to decrease the detection loss (connecting to external PDs needs the usage of grating couplers with considerable losses), increase the signal stability (because no fiber is used), and reduce the size of the entire system. Our on-chip six-beam LDV is much smaller than conventional discrete-optics LDVs (e.g. Polytec MPV-800) and fiber LDVs. The footprint of the our 6-beam LDV PIC (including PDs) is only  $2.5 \text{ mm} \times 5 \text{ mm}$ . The SOI technology also ensures a low production cost, even at moderate production volume. The SOI waveguides are not transparent to light in the visible range, therefore an infrared wavelength (1550 nm) is used. The disadvantages of using infrared light include the invisibility of the beams and strong absorption in water. However, a high eye-safe power and a long coherence length make the 1550 nm light a good candidate for many applications, e.g. a long-distance measurement [12].

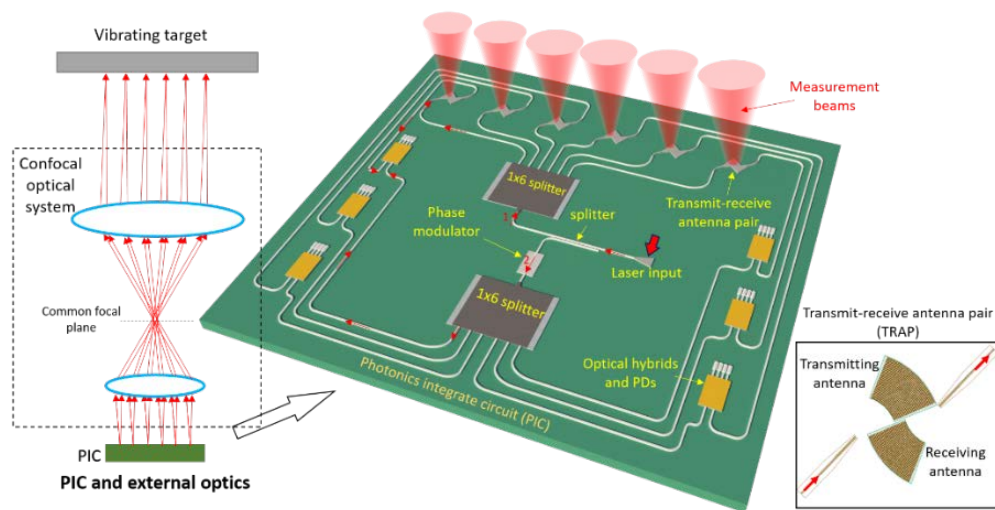


Fig. 1. Schematic show of the external confocal optical system, the six-beam LDV on an SOI-based photonic integrate circuit (PIC) and a transmit-receive antenna pair. The drawing of the confocal system is exaggerated to make the design easier to understand.

## 2. PIC design and packaging

The PIC with a six-beam LDV is schematically shown in Fig. 1. 1550 nm light is delivered to the PIC via a grating coupler (insertion loss  $\approx 3\text{dB}$ ) from an external laser (Eblana EP-1550-DM). The linewidth of the light is around 800 kHz, corresponding to a coherence length of 120 m. In the PIC, an on-chip directional coupler splits the light power into two parts. Approximately 80% of optical power goes to the measurement waveguide (direction 1 in Fig. 1) and the rest goes to the reference waveguide (direction 2 in Fig. 1). On one hand, the measurement signal is evenly split into six parts via a  $1 \times 6$  multimode-interference (MMI) coupler, and then reaches six transmitting antennas (TAs), where they are coupled out of the

PIC to the target. The TAs use the reflectionless grating coupler design [13], which keeps the grating-induced spurious reflections from going back to the entrance waveguide to avoid the non-linear effects in the LDV outputs caused by these spurious reflections. To ensure that enough useful reflection is collected back to the PIC, a confocal optical imaging system is placed in front of the TAs. The confocal system focuses the light beams onto the target and collects corresponding reflections back to the six receiving antennas (RAs), which are adjacent to the corresponding TAs. In order to keep a small distance between the TAs and RAs, the RA designs are rotated by  $180^\circ$  w.r.t. the TAs (see Fig. 1). The transmit-receive antenna pairs (TRAPs) are similar to the “2gc” antennas presented in [8]. On the other hand, the reference signal is also split into six parts with the aforementioned  $1 \times 6$  MMI design so that each reflection signal can be combined with one reference signal into a 90-degree optical hybrid [8]. A 90-degree optical hybrid provides four mixture signals in quadrature, i.e. the phase differences in these signals ( $\varphi$  in Eq. (2)) can be expressed as  $\varphi_k = \varphi_0 + k \cdot 90^\circ$ , where  $k = 0,1,2,3$  is the index of the port. The four outputs of each 90-degree optical hybrid are connected to four on-chip germanium PDs with a responsivity of about 1 A/W and a bandwidth higher than 1 GHz [9]. The PD responsivity is measured in a structure where the PD is connected to a standard grating with a known coupling efficiency ( $\sim 2.5$  dB). The four PDs are connected to five bonding pads with one common anode (see Fig. 2). Under zero bias, the photocurrent signals from the four PDs are sent to four trans-impedance amplifiers (TIAs) via bonding wires. Thanks to the 90-degree optical hybrid, the four photocurrent signals can be represented by

$$sig_{m,k}(t) = dc_m + r_m \cdot \cos[k \cdot 90^\circ - \theta_{Doppler,m}(t) + \varphi_m] \quad (3)$$

where  $m$  ( $= 1,2,3,4,5,6$ ) denotes the index of the six channels. These TIAs are located relatively close to the PDs to prevent the photocurrents from picking up too much noise before amplification. After the first-stage amplification, 12 second-stage differential amplifiers are placed to remove the common voltage in the complementary signals (e.g.  $k = 0$  and  $k = 2$ ). After this stage, six  $I$  signals, i.e.  $I_m(t) = sig_{m,0}(t) - sig_{m,2}(t) = 2r_m \cdot \cos[\theta_{Doppler,m}(t) - \varphi_m]$ , and six  $Q$  signals, i.e.  $Q_m(t) = sig_{m,1}(t) - sig_{m,3}(t) = 2r_m \cdot \sin[\theta_{Doppler,m}(t) - \varphi_m]$ , are obtained, with the common signals  $dc_m$  mostly removed. These  $IQ$  signals are then sent to an arctan decoder for signal recovery, i.e.  $\theta_{Doppler,m}(t) = \arctan[Q(t)/I(t) + \varphi_m]$ . Six displacement or velocity signals are finally obtained.

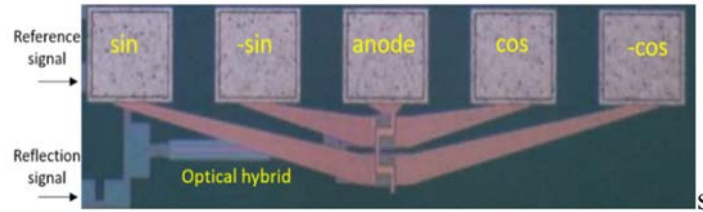


Fig. 2. Microscopic image of a 90-degree optical hybrid with four connected PDs and their corresponding bonding pads. The width of each pad is  $100 \mu\text{m}$ , and their spacing is  $50 \mu\text{m}$ .

Due to a slight imbalance among the output ports of the 90-degree optical hybrid, the dc signals in the photocurrents usually cannot be completely removed after the differential amplifiers. Hence a center-searching post-processing is needed to remove the residual dc signals. The center-searching algorithm performs well when the target displacement amplitude is larger than  $\lambda_0/2$ , meaning that the  $IQ$  Lissajous traces is a complete circle. But when the target's movement is so small that the Lissajous figure becomes an incomplete circle, this algorithm may fail to find the center of the circle. To avoid such problems, we put a phase modulator that can induce a  $2\pi$  phase shift on the reference arm to create a complete  $IQ$  circle. The thermo-optic phase modulator is placed on the common waveguide shared by

the six reference signals. This phase modulator is realized by using a heavily p-type doped silicon wire (cross-section:  $1.2 \mu\text{m} \times 220 \text{ nm}$ , length:  $150 \mu\text{m}$ ) as a heater, which is placed next to the reference waveguide to modulate its temperature. According to the thermo-optic effect, the refractive index of the reference waveguide can be modulated as a result of the temperature change, which finally leads to a phase modulation. The gap between the heater and the reference waveguide is set as  $0.6 \mu\text{m}$  to compromise between a small optical cross-talk and a high temperature modulation efficiency. To even enhance the maximal modulation of the phase, the reference waveguide is bent in such a way that it is placed on both sides of the heater. The measured resistances of the heaters are between  $14 \text{ k}\Omega$  and  $15 \text{ k}\Omega$ . The modulation ability is tested in a Mach-Zehnder interferometer, showing that a  $15 \text{ V}$  voltage is needed to realize a  $2\pi$  phase shift in the reference waveguide. The rise time (90%) from 0 to  $2\pi$  is between  $15 \mu\text{s}$  and  $20 \mu\text{s}$ . Another function of the phase modulator is to synchronize the six outputs since it is shared by all reference signals.

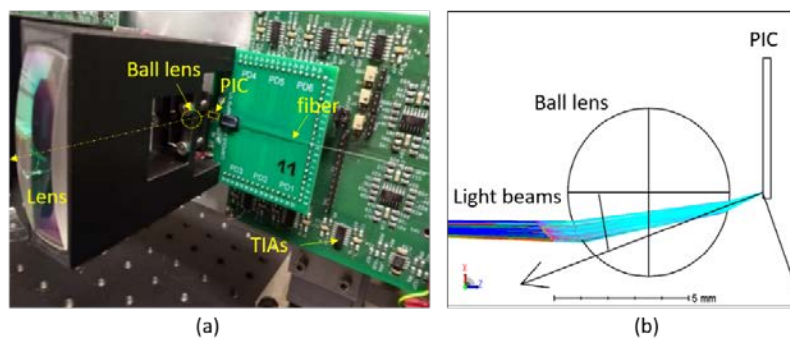


Fig. 3. (a) Image of the six-beam LDV. The input fiber, the supporting PCBs and the confocal systems (the front lens was cut to reduce the size of the system) are shown. (b) Schematic show of the shifted confocal system. It is clearly seen that the ball lens is shifted to ensure that the beams passing through the ball lens are perpendicular to the PIC surface.

The confocal optical system is designed to ensure that the six outward beams are parallel and focused to the target with a predefined spacing ( $5 \text{ mm}$ ). Our confocal system consists of a ball lens with  $6 \text{ mm}$  diameter (Edmund optics 32-746) and a Bi-convex lens with a focal length of  $75.0 \text{ mm}$  (Thorlabs LB1309-C) (see Fig. 3(a)). One issue of the system is that the output beams of the TAs have a  $10^\circ$  angle relative to the PIC normal, which is designed to avoid 2nd order reflections in the grating couplers. To ensure the six output beams are perpendicular to the surface of the PIC, the confocal system is slightly shifted relative to the TAs (see Fig. 3(b)). Besides, the decentering of the ball lens also helps to avoid strong spurious reflections originated from the ball lens surface, which is not treated with any anti-reflective layer. The transmission efficiency of this optical system is validated with a ray-tracing method (Zemax OpticStudio), which shows that the confocal optics delivers around 83% of light power to the target (forward direction). The loss is mainly caused by the surface reflection at the glass/air interfaces, since no anti-reflective layer is considered in the simulation. If a micro-bead based retro-reflector with  $50 \mu\text{m}$  ball diameter is used, around 6% of light incident on the target can be sent back to the receiving region of the RAs (for the strongest reflection point in the retroreflector). The loss is mainly due to scattering loss in the retroreflectors. Due to the phase mismatch between reflected signal and grating coupler mode, an extra loss should also be considered. Therefore, the power reflected to the PIC is even less. However, despite all these losses, the LDV still works well.

Since the light is infrared, a pair of aiming beams is also attached to the system, indicating the focal plane of the output beams.

### 3. Results and discussion

In the measurement, the input optical power (before the input grating coupler) was set to around 8 mW. Measurements showed that the forward loss (from the input grating coupler to the output beams) was around 8 dB, including losses in the input grating coupler (~3 dB), in the 20:80 splitter (~1.5 dB), in the  $1 \times 6$  splitter (~1.5 dB) and in the TAs (~2 dB). The backward loss (from the target back to the waveguide) was at least 2 dB (best coupling efficiency of the RAs), but was normally much higher due to the scattering in the target. This value depends on the reflector type. For example, the measured backward loss of a micro-bead retro-reflector (with bead radius of around 50  $\mu\text{m}$ ) was at least 22 dB. This retro-reflector was used in the measurements described below. The spectrum of a displacement with a 61.5 kHz frequency and a 66 nm amplitude is shown in Fig. 4. The displacement resolution of the LDV was estimated by calculating the noise floor of the demodulated signals, which corresponds to a displacement amplitude of less than 10 pm with a resolution bandwidth of 0.445 Hz. The resolution has not reached the state-of-art mainly due to the instability of the laser (e.g. large linewidth), discretization errors in the data-acquisition (DAQ) system, and the electronic 1/f noise. Also note that the resolution for infrared light is usually worse than that for red light, since infrared light has a longer wavelength (see Eq. (1)). The LDV resolution can be improved further by increasing the input optical power, decreasing the laser linewidth, or improving the DAQ resolution. Another method is to use a heterodyne method, which can considerably remove the impact of the 1/f noises.

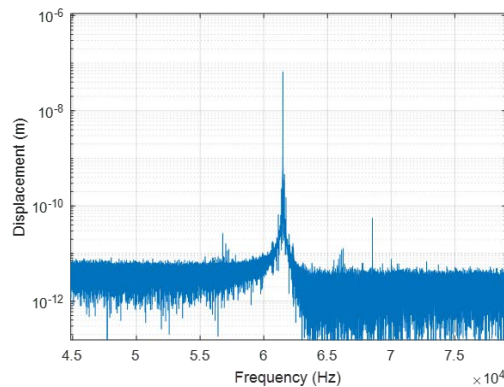


Fig. 4. The displacement spectrum of the LDV output when it is measuring an aluminum plate vibrating at 61.5 kHz. The resolution bandwidth is 0.445 Hz.

The crosstalk between each channel should be low enough to avoid output distortions. In this design, the separation of two adjacent TAs is kept relatively large (300  $\mu\text{m}$ ) compared to the effective size of the TA (10  $\mu\text{m}$ ) to avoid possible crosstalk. We measured the crosstalk by placing a small piece of reflector in the focus plane of the LDV and only reflecting one chosen beam. Results show that the photocurrents in the other channels are lower than the noise floor.

To demonstrate the simultaneous multi-channel measurements with our device, we measured high-frequency elastic waves which propagate in an aluminum plate (thickness of 1.45 mm). In these measurements, we fixed the lower part of the plate and placed a circular piezoelectric PZT actuator (diameter = 20 mm) in the center of the plate (see Fig. 5). Beneath the PZT patch, four pieces of retroreflectors were placed to enhance the reflection of the four measurement beams (#1, #2, #4, and #6 of the six beams). The spacing of these four beams were 5 mm, 10 mm and 10 mm, respectively. We did not use all six channels because of the channel limitation of our high-speed DAQ card (NI USB-6356). The signals were captured at a sampling rate of 1 Msps. A 4-cycle sine burst (voltage of 150 Vpp) at a certain frequency (i.e. 31.5 kHz, 41.5 kHz, ... 91.5 kHz) was fed to the PZT patch (see Fig. 5). The interval

between two adjacent sine bursts was 200 ms. The PZT patch induced a dispersive elastic wave with circular phase front which thus traversed the four retroreflectors. With this settings, we were mainly stimulating the fundamental antisymmetric  $A_0$  Lamb wave at a certain frequency-thickness product ( $fd$ ) [14]. The size of the aluminum plate is selected to be large enough so that the first groups of waves coming from the PZT and the reflection waves from the different edges of the plate can be well separated in the time domain. This ensures a time region that only the first group of the forward waves exists, which can be used the phase velocity calculation.

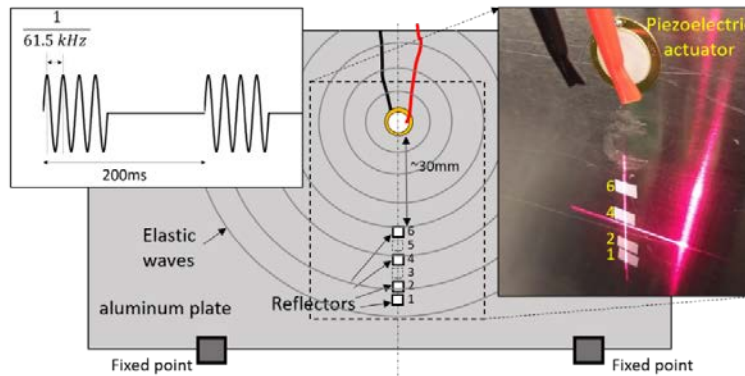


Fig. 5. The aluminum plate used in the measurement. The input voltage to the piezo actuator is shown on the top-left corner. The image of the piezo actuator and the positions of the reflectors in shown in the top right corner. The red crosses are the aiming beams.

When input frequency was 61.5 kHz,  $fd = 61.5 \text{ kHz} \times 1.45 \text{ mm} \approx 89 \text{ kHz} \cdot \text{mm}$ . The corresponding out-of-plane surface velocities (with a band-pass filter between 51.5 kHz and 71.5 kHz) measured by the four beams are shown in Fig. 6(a). The amplitudes of the corresponding displacements are between 4 nm and 6.5 nm. There are clearly two sets of waves propagating in the opposite directions. In the time region with only the first group of forward waves, a cross-correlation method is applied between two different signals to retrieve the corresponding time differences. From these time differences, we can calculate the propagation speed to be  $909 \pm 17 \text{ m/s}$ . Here, the error is estimated based on the time resolution of the DAQ. The distances between any two measuring positions may also be different from expectations. This leads to another possible error in the calculated velocity. This dislocation error is estimated to be less than 4% by measuring the location deviations of the six infrared beams on the target with the help of an infrared detector card. The dislocation error will cause an overall increase or decrease of the measured velocity values.

Since there are several cycles in one burst, the propagation speed should be close to the phase velocity of the wave. The computed dispersion curve, describing the phase velocity  $c_{ph}$  dependency on the frequency-thickness product  $fd$  [15], is shown in Fig. 6(b) for the  $A_0$  Lamb mode in an aluminum plate. For the aluminum, following mechanical parameters have been assumed: density  $\rho = 2700 \text{ kg/m}^3$ , Young's modulus  $E = 70 \text{ GPa}$  and Poisson coefficient  $\nu = 0.33$ . The phase velocities derived from the forward waves of our measurement results at different frequencies are shown in the same figure. Note that the pass-bands of the filters applied to these vibrations are kept as small as 2 Hz to ensure the calculated values are phase velocities. It turns out that our measurement results at different frequencies are very close to the theoretical predictions (e.g.  $c_{ph} = 906.7 \text{ m/s}$  @ 61.5 kHz) only considering the errors caused by the DAQ resolution. The errors related to the distance deviations are not apparent since the measurement data are well fitted to the theoretical prediction. The discrepancy may also be attributed to possible deviations in the actual mechanical parameters of the aluminum plate, and to the impact of the attached retroreflectors.

The backward wave in Fig. 6(a) is the reflection of the forward wave, e.g. at the bottom edge of the aluminum plate. It has the same speed as the forward wave. However, since many places can introduce reflections, the observed backward wave may be a combination of many reflections, which makes the backward wave not so easy to analyze. However, the observation of the propagation direction of a wave demonstrates the advantage of the multi-beam LDV, which cannot be realized with a single beam LDV.

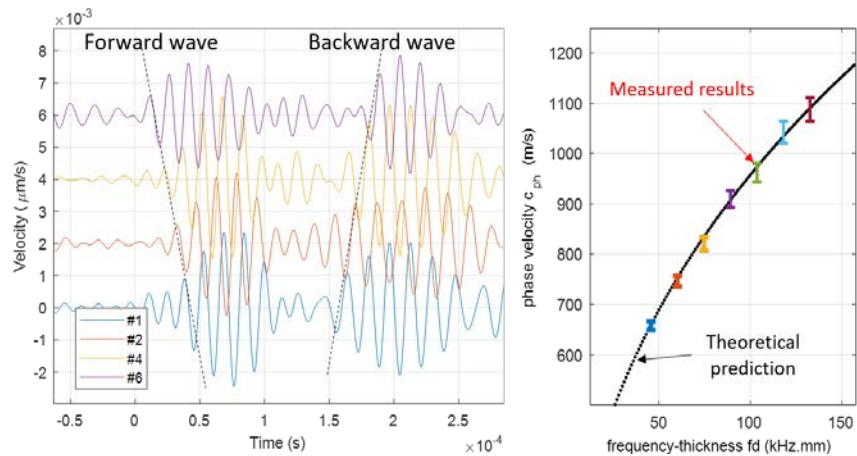


Fig. 6. (a) The out-of-plane surface velocities at the four reflectors as function of time. The velocities of #2, #4 and #6 are shifted to ensure the curves are clearly distinguished. (b) Theoretical dispersion curve of the  $A_0$  Lamb wave for aluminum, with the experimental measurement results superimposed. The error bars are calculated according to the time resolution of the DAQ.

#### 4. Conclusion

We have reported a six-beam LDV integrated on SOI with integrated photo-diodes. The footprint of the photonic IC for the six-beam LDV is  $2.5 \text{ mm} \times 5 \text{ mm}$ , and it is packaged with a laser source, amplification electronics, an external confocal optical system and two aiming beams. We show experimentally that the six-beam LDV can work simultaneously to record the propagation of an elastic wave, and estimate its phase velocity (around  $909 \text{ m/s}$  @  $61.5 \text{ kHz}$ ).

#### Funding

European Horizon 2020 project CARDIS (Project 644798).

#### Acknowledgments

The authors thank Dr. Stephane Clemmen for his technical support.